

1
2
3
4
5
6
7
8
9
10
11
12
13
14
15
16
17
18
19
20

Conduction Velocities of Excitatory Axons Innervating Parvalbumin Interneurons in Primary Somatosensory Cortex

Kate Scheuer¹

Xinyu Zhao^{2,3}

Meyer Jackson³

1. Cellular and Molecular Biology Program, 2. Waisman Center, and 3. Department of Neuroscience, University of Wisconsin-Madison, Madison, Wisconsin 53705

Corresponding author email: meyer.jackson@wisc.edu

Conflict of interest statement: The authors declare no competing financial or non-financial interests.

Acknowledgements: National Institutes of Health Grants NS105200 and NS093866 to M.B.J. and X.Z. Thanks to Dr. Shane McMahon for methodological contributions.

21 **Abstract**

22 Timing plays a critical role in signaling throughout the nervous system. Signaling times
23 vary widely depending on distance and speed, and timing delays influence circuit computations
24 such as coincidence detection, synaptic integration, entrainment, temporal summation, and
25 plasticity. Parvalbumin (PV) interneurons are a major type of inhibitory neuron with critical roles
26 throughout the brain. Their rapid-spiking characteristics enable them to control the dynamics of
27 neural circuits across a range of time scales. However, little is known about the factors that
28 determine the timing of their synaptic inputs. Here, we measured the conduction velocity (CV) of
29 excitatory axons that target PV interneurons in mouse primary somatosensory cortex. Using a
30 genetically-encoded hybrid voltage sensor (hVOS) targeted to PV interneurons, we clocked the
31 arrival of excitatory synaptic inputs with sub-millisecond precision in large numbers of cells
32 across multiple layers. Arrival times varied with distance, allowing us to determine the CV of the
33 excitatory axons. Values ranged from 28–241 $\mu\text{m}/\text{msec}$ across layers 2-5, and interlaminar CV
34 was about twice as fast as intralaminar CV. This will enable more rapid computation within
35 columns, while integration between columns will be slower. hVOS imaging from specific cell
36 types offers a unique opportunity to investigate conduction in axons defined by their targets.

37

38 **Introduction**

39 Axonal conduction velocity (CV) influences neural computations by controlling the
40 timing of synaptic inputs. CV impacts processes such as coincidence detection, temporal
41 summation, entrainment, oscillations, synaptic integration, and synaptic plasticity (Bucher &
42 Goaillard, 2011; Chomiak, Peters, & Hu, 2008; Fields, 2015; Pajevic, Basser, & Fields, 2014;
43 Salami, Itami, Tsumoto, & Kimura, 2003). Small variations in CV can have a profound impact
44 on synchrony and oscillation frequency (Ivanov, Polykretis, & Michmizos, 2019; Pajevic et al.,
45 2014), and CV alterations have been linked to a variety of diseases including diabetes (Candy &
46 Szatkowski, 2000), schizophrenia (Corcoba et al., 2015), and Down Syndrome (Olmos-Serrano
47 et al., 2016). Demyelination associated with degenerative diseases such as multiple sclerosis has
48 a major impact on CV (Compston & Coles, 2002; Nave, 2010; Pedroni, Minh do, Mallamaci, &
49 Cherubini, 2014), and slower CV caused by decreased erbB signaling has been linked to bipolar
50 disorder and schizophrenia (Roy et al., 2007).

51 CV is determined by axonal diameter and other geometric properties, as well as the
52 capacitance and intrinsic excitability of the axonal membrane. CV varies widely between
53 different axons and functional pathways. Axons projecting from ventral temporal cortex to the
54 inferior colliculus conduct approximately three times faster than those projecting to caudate
55 putamen (Chomiak et al., 2008), and hippocampal dentate granule cell (mossy fiber) axons
56 conduct more rapidly than the axons of hilar mossy cells (Ma, Bayguinov, & Jackson, 2017). CV
57 can also differ within the axons of the same cell. For a given ventral temporal cortical neuron,
58 axonal branches with contralateral targets have significantly slower CV compared to axonal
59 branches with ipsilateral targets (Chomiak et al., 2008). CV may also vary based on postsynaptic
60 cell type. As a result of differences in CV, stimulating the same thalamic neuron activates

61 inhibitory targets before excitatory targets in somatosensory barrel cortex (BC), thus setting a
62 very narrow time window for excitation (Kimura et al., 2010). Additionally, cell type can
63 influence CV variability. Martinotti cells in layer 5 (L5) BC have more variable axonal CVs
64 compared to pyramidal cells in the same layer (Shlosberg, Abu-Ghanem, & Amitai, 2008). These
65 many variations in CV determine not only computation speed, but by influencing timing and
66 delays, determine how circuits encode and process information.

67 Previous measurements of CV have been hindered by technical constraints arising from
68 the difficulty of recording directly from axons, as well as low throughput, and lack of spatial and
69 temporal resolution. Voltage imaging has provided a powerful general method for the
70 measurement of axonal CV (Grinvald, Ross, & Farber, 1981; Hamada, Popovic, & Kole, 2017;
71 Popovic, Foust, McCormick, & Zecevic, 2011; Sakai et al., 1991), and genetically-encoded
72 voltage indicators have extended the approach to these problems through the addition of
73 targeting specificity (Ma, Bayguinov, & Jackson, 2019; Panzera & Hoppa, 2019). The hybrid
74 voltage sensor (hVOS) has sub-millisecond temporal resolution, single-cell spatial resolution
75 (Chanda et al., 2005; Ghitani, Bayguinov, Ma, & Jackson, 2015; Ma et al., 2017), and can be
76 targeted to specific cell populations (Bayguinov, Ma, Gao, Zhao, & Jackson, 2017; Chanda et al.,
77 2005; Ghitani, Bayguinov, Ma, & Jackson, 2015; Ma et al., 2017). hVOS reveals voltage
78 changes from large numbers of neurons simultaneously, and when targeted directly to axons, can
79 resolve differences in CV based on cell type (Ma et al., 2017). In this study, we used hVOS to
80 measure CV along excitatory axons targeting inhibitory parvalbumin (PV) interneurons in mouse
81 BC. Because they fire rapidly and have a short membrane time constant, PV interneurons play a
82 critical role in controlling the temporal integration window of their targets (Cardin, 2018;
83 Ferguson & Gao, 2018; Galarreta & Hestrin, 2002; Pouille & Scanziani, 2001). They are also

84 essential for the generation of gamma oscillations, rhythmic brain waves between 30 and 80 Hz
85 which affect sensory integration, working memory, social cognition, and other functions
86 (Gandal, Edgar, Klook, & Siegel, 2012; Gloveli et al., 2005; Gonzalez-Burgos, Cho, & Lewis,
87 2015; Pouille & Scanziani, 2001). Both PV interneurons and gamma oscillations have been
88 implicated in a variety of psychiatric and neurological disorders including schizophrenia, bipolar
89 disorder, and autism spectrum disorder (Gonzalez-Burgos et al., 2015; Lauber, Filice, &
90 Schwaller, 2018; T. Y. Liu et al., 2012). The fast-spiking behavior of PV interneurons suggests
91 that they are adapted to rapid computations. Thus, the speed of their activation by excitatory
92 inputs is likely to be important to their function.

93 While PV interneurons are present throughout L2-6, their density and circuitry vary
94 widely within the cortex (Staiger & Petersen, 2021). Properties such as excitation/inhibition
95 balance and gamma oscillation frequency, both linked to PV interneuron function, differ based
96 on cortical layer (Adesnik, 2018; Xu et al., 2016). We used the response latencies of PV
97 interneurons to determine CV within and between different cortical layers. CV varied widely
98 from $44 \pm 15 \mu\text{m}/\text{msec}$ (mean \pm SD) for L2/3 intralaminar CV to up to $241 \mu\text{m}/\text{msec}$ for L5 \rightarrow
99 L4 CV. The mean interlaminar CV ($111 \pm 49 \mu\text{m}/\text{msec}$) was about twice as fast as the mean
100 intralaminar CV ($57 \pm 41 \mu\text{m}/\text{msec}$). These differences between inter- and intralaminar CV will
101 influence processing within the BC to make computations within columns faster than
102 computations between columns.

103

104

105 **Results**

106 *PV interneuron responses to stimulation in L2/3, L4, and L5*

107 In mice from PV-Cre crosses with hVOS Cre reporter mice (see Methods), hVOS probe
108 has been shown to be expressed in 83% of PV interneurons with 99.2% specificity (Bayguinov et
109 al., 2017). In slices from these mice, BC cortical layers and barrels are visible in gradient
110 contrast optics (Fig. 3A) and fluorescence (Fig. 3B; note that the images were taken with
111 different cameras, so the fields of view do not align precisely). Layers were identified by cell
112 density and cell size (Feldmeyer, 2012; Woolsey & Van der Loos, 1970), and boundaries
113 between layers are marked with dashed lines (Figs. 1, 3, 4, Supp. Fig. 1). Fields of view
114 generally contained L2/3 through L5 (Fig. 1). Barrels were separated into faint “hollows”
115 (Feldmeyer, 2012; Woolsey & Van der Loos, 1970) as well as stronger fluorescence in L4, and
116 boundaries between columns marked by dotted lines (Fig. 3, 4, Supp. Fig. 1). Electrical
117 stimulation in L2/3, L4, and L5 elicited voltage changes in PV interneurons distributed through
118 L2-5, as shown in the maximum amplitude heatmaps in Figs. 1A (L2/3), 1B (L4), and 1C (L5).
119 Warmer colors correspond to greater changes in fluorescence and indicate the presence of
120 responsive PV interneurons. Traces from locations (indicated by number and color) reveal
121 corresponding variations in the magnitude of PV interneuron depolarization (Fig. 1D-F). Dark
122 blue regions of the heatmap indicate the absence of responsive PV interneurons, and traces from
123 those locations show no discernable stimulus-evoked fluorescence change.

124

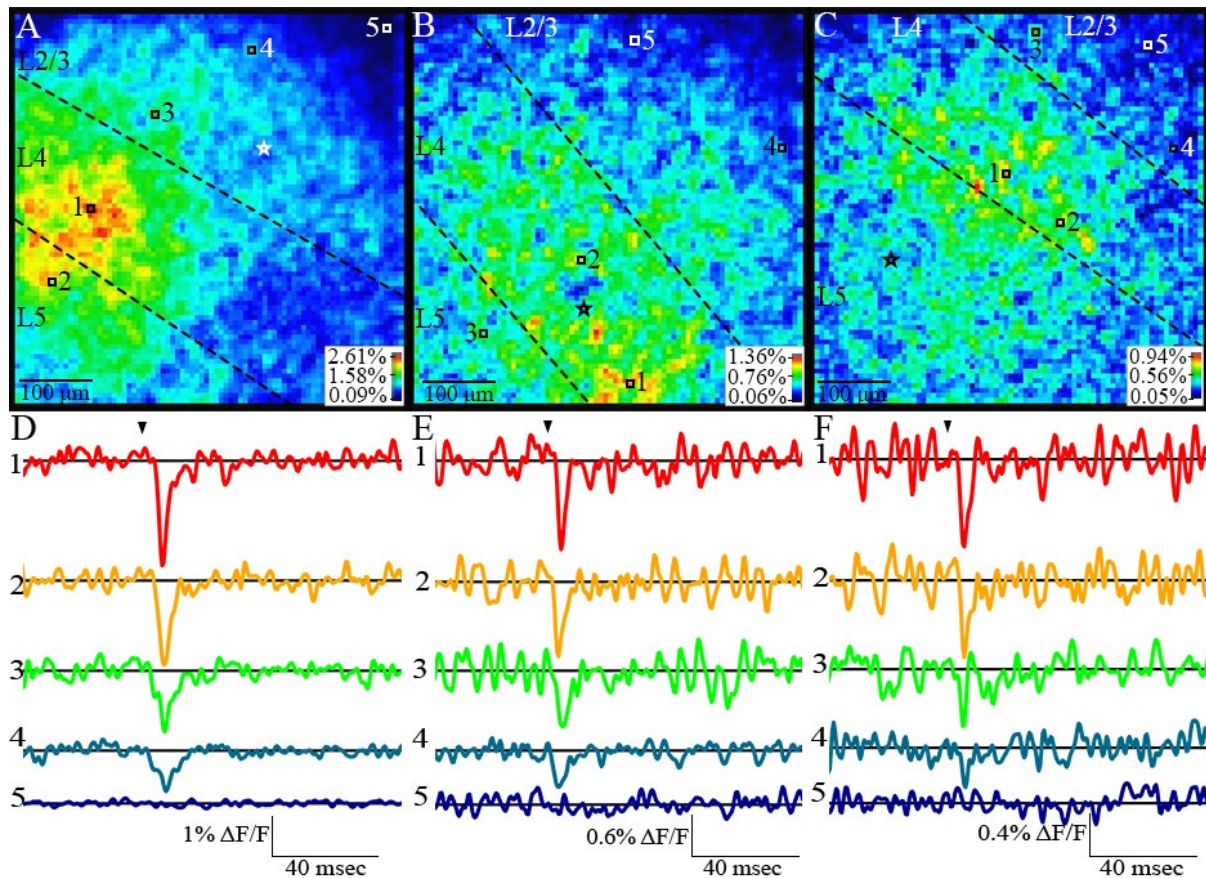


Figure 1. PV interneurons throughout a slice respond to stimulation in L2/3 (A), L4 (B), L5 (C) (stimulation sites indicated by white or black stars). In maximum amplitude heatmaps, warmer colors indicate greater changes in fluorescence. These differences in amplitude are visible in selected traces of fluorescence versus time (D-F) from the corresponding heatmaps above. Locations of traces are indicated with small white or black squares and numbers in each map. Arrowheads indicate time of stimulation.

125 Stronger stimulation elicited responses in more cells over greater distances. Heatmaps of
126 signal-to-noise ratio (SNR) revealed that stimulation with 10 μ A rarely elicited detectable
127 responses (Fig. 2A). Increasing the stimulus current to 20 μ A (Fig. 2B) and 60 μ A (Fig. 2C)
128 elicited responses in more neurons over greater distances, and increasing to 100 μ A depolarized
129 still more neurons over a broader range of distances encompassing nearly the entire field of view
130 (Figs. 1, 2D). Responses depended on synaptic excitation, as they were blocked by 10 μ M
131 NBQX (Figs. 2E-2F). Patterns of response spread varied but often included intralaminar
132 responses across multiple barrel columns (Video 1) and/or interlaminar responses within and
133 between barrel columns (Videos 2, 3). These excitatory responses spread away from the stimulus

134 electrode as action potentials propagated along excitatory efferents; the speed of this spread
135 reflects the CV along these axons.

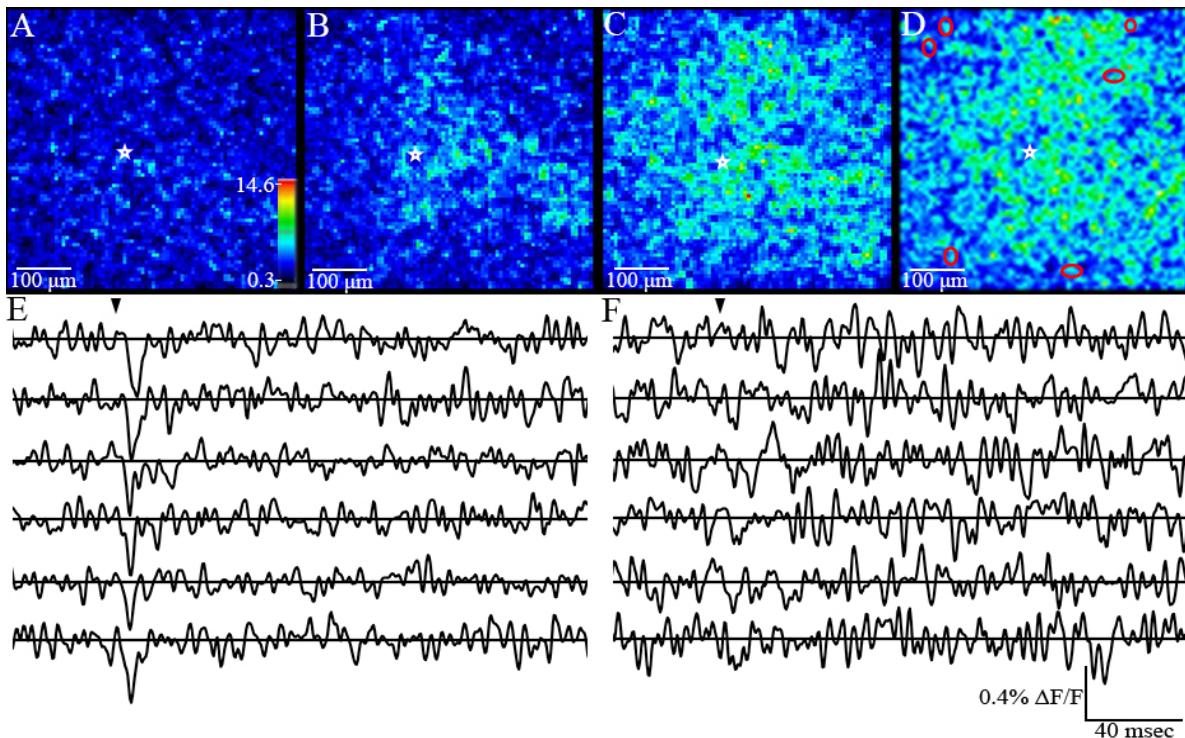


Figure 2. PV interneuron responses to different stimulation currents. Heatmaps of SNR following stimulations of 10 μA (A), 20 μA (B), 60 μA (C), and 100 μA (D). Site of stimulation is marked with a white star in A-D. Heatmap scale in (A) also applies to (B-D). A method of analysis was developed to identify individual, non-overlapping cells with clear responses (see Methods for criteria). E-F. Traces from 6 clearly identified PV interneurons (circled in red in D) show fluorescence versus time before (E) and after (F) the addition of 10 μM NBQX. Blockade by NBQX indicates that responses are glutamatergic.

136 *Identification of single PV interneurons*

137 Determining CV requires the observation of responses in significant numbers of clearly
138 identified neurons with well-resolved locations and accurately measured latencies. Fluorescence
139 images of slices (Fig. 3B) display diffusely distributed fluorescence due to the dense arborization
140 of PV interneurons (Fukuda & Kosaka, 2003). This makes it difficult to locate individual cells
141 precisely. This, together with the large numbers of responsive cells, made manual analysis
142 extremely time-consuming. We therefore developed a semi-automated method to identify
143 responsive PV interneurons (see Methods and Supp. Fig. 1). Briefly, pixels above a baseline
144 SNR cutoff (Supp. Fig. 1A) were divided into groups using k-means clustering of the SNR maps

145 (Supp. Fig. 1B). Putative somata were identified as contiguous groups of pixels in the same k-
146 means cluster based on the reasoning that pixels from the same cell body are expected to have a
147 similar SNR. A pixel group was considered to be a PV interneuron soma if its amplitude and
148 SNR were above the cutoffs (0.1% for amplitude, 5 for SNR), did not share a face with another
149 pixel group, and was $< 20 \mu\text{m}$ across (consistent with the size of a PV interneuron soma
150 (Kooijmans, Sierhuis, Self, & Roelfsema, 2020; Selby, Zhang, & Sun, 2007; Y. Wang, Gupta,
151 Toledo-Rodriguez, Wu, & Markram, 2002)).

152 This process provided a reproducible, robust method of identifying individual PV
153 interneurons free of subjective choices. The procedure is illustrated with a slice from which a
154 gradient contrast image is shown in Fig. 3A and a resting fluorescence image is shown in Fig.
155 3B. The electrode, visible in L2/3 in both images, was used to apply a stimulation of $100 \mu\text{A}$. A
156 SNR heatmap revealed activated cells concentrated in L4, but cells in L2/3 and L5 also
157 responded (Fig. 3C). This heatmap highlights 56 PV interneurons identified with our clustering
158 method. Responsive neurons were outlined in black, or in red for locations selected for display of
159 fluorescence versus time (Fig. 3D). The 8 selected traces show clear depolarizing responses
160 following stimulation.

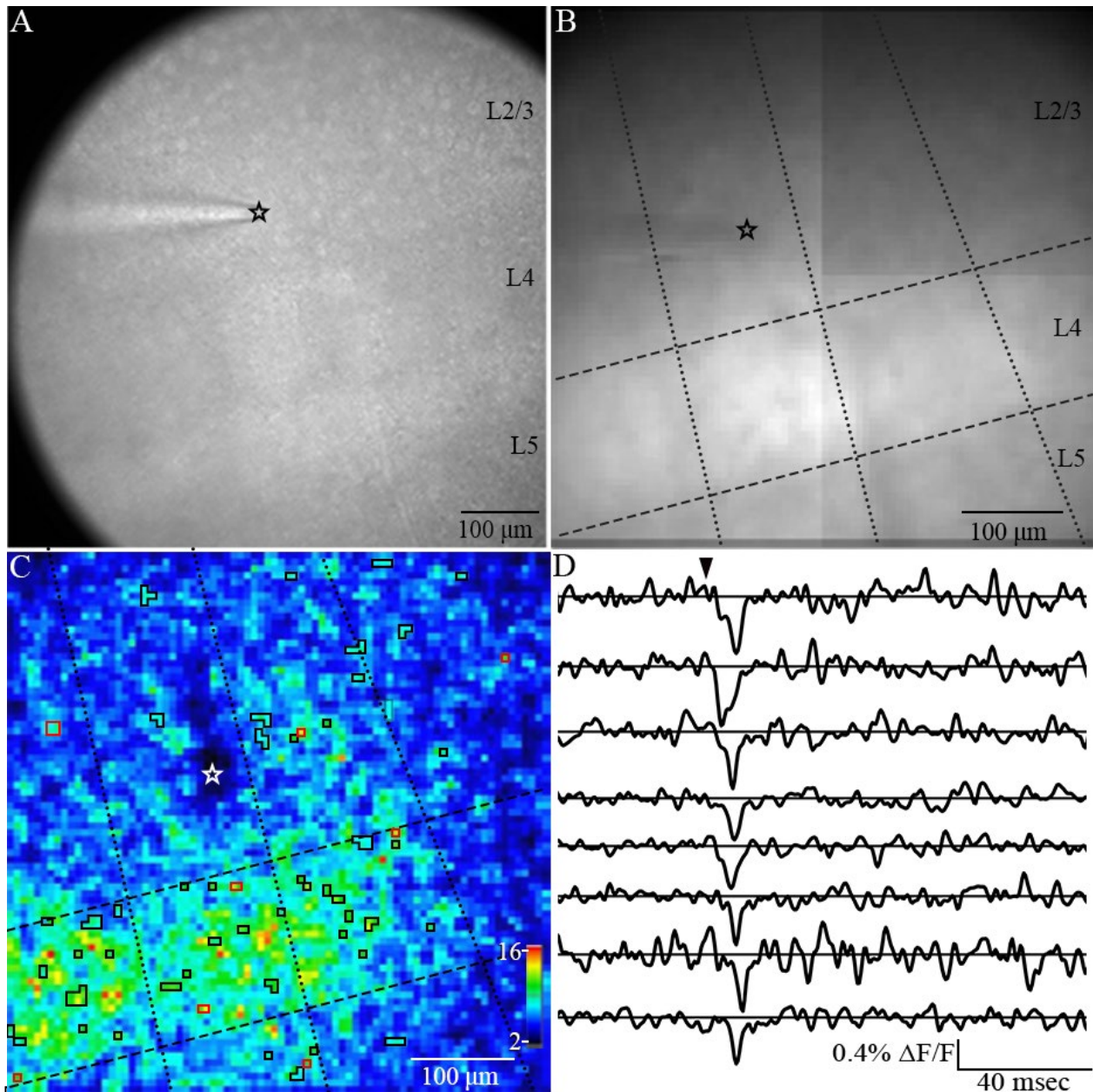


Figure 3. Identification of responsive PV interneurons. A. Gradient contrast image (taken with the Kiralux camera), and B. fluorescence image (taken with the CCD-SMQ camera) of a BC somatosensory cortical slice containing L2/3, L4 and L5. The stimulating electrode is visible in L2/3 (star at the tip, black in A and B, white in C). Layer boundaries are indicated by dashed lines, and barrel column borders are indicated with dotted lines in B-C. Following 100 μ A stimulation, responsive PV interneurons were identified based on K-means clustering of SNR and other criteria (see Methods and Supp. Fig. 1). C. A SNR heatmap shows that responsive PV interneurons span the field of view and are present in L2-5. We identified 56 responsive PV interneurons outlined in black or red. D. Traces of fluorescence versus time for the 8 PV interneurons outlined in red in C. Arrowhead above indicates stimulation time. All displayed traces show clear decreases in fluorescence following stimulation, indicating depolarization of the highlighted PV interneurons.

161 Returning to Fig. 2, this method identified 12, 96, 176, and 115 responsive PV
162 interneurons for 10, 20, 60, and 100 μ A stimulation, respectively. The decrease in number of

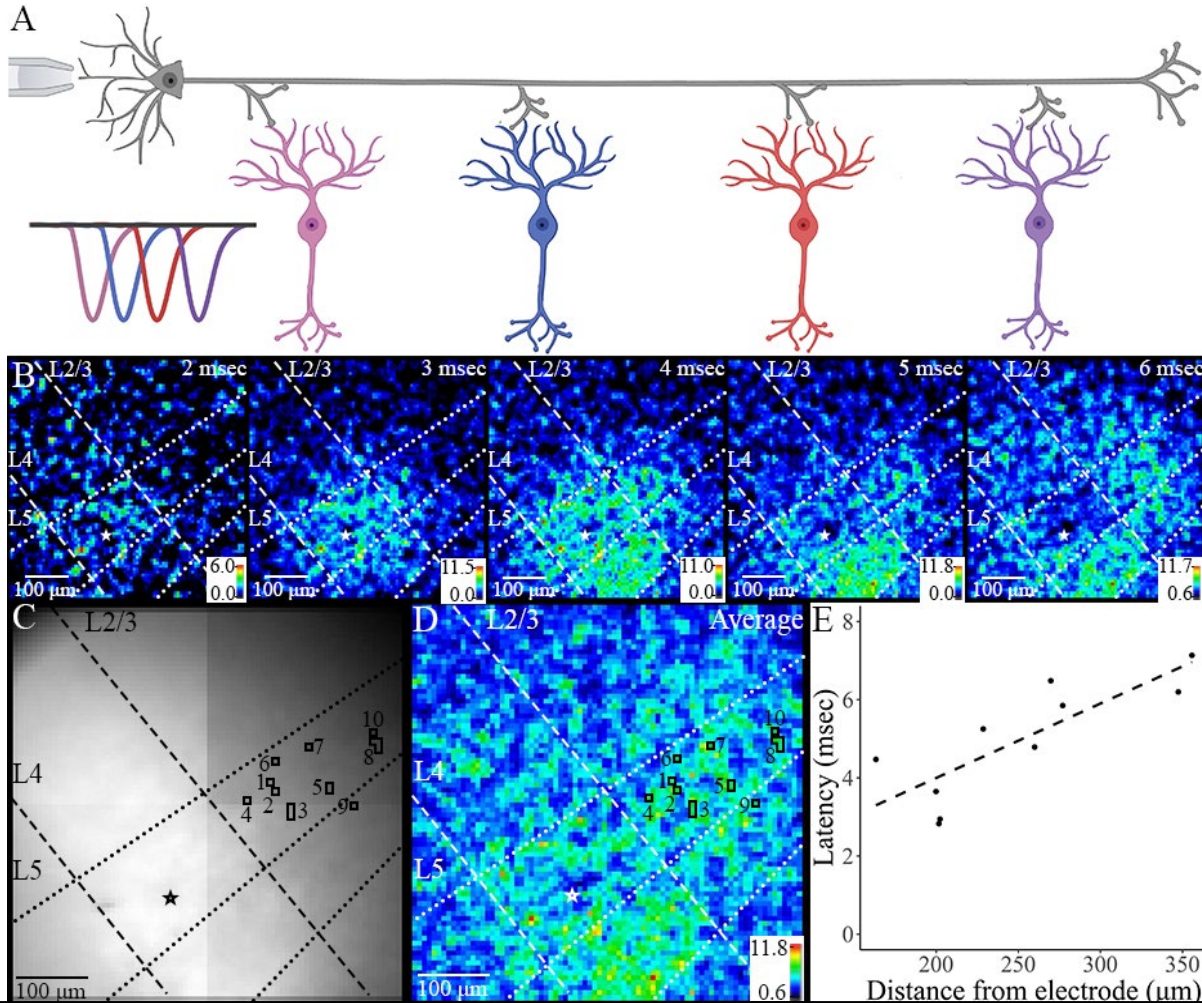
163 identifiable cells with 100 μ A reflects the higher proportion of overlapping cells that could not be
164 disambiguated. The best balance between extensive spread with large numbers of readily
165 resolved individual cells versus too much overlap was seen with 100 μ A, so this stimulus
166 strength was used for experiments on CV. The broad patterns of propagation are clearly evident
167 in unprocessed data as illustrated in the heatmaps and supplemental videos described above.
168 However, by employing method we were able to focus on somata and improve the precision of
169 latency determination. We were thus able to analyze large numbers of cells over a broad area
170 with a wide range of propagation distances. This analysis thus provided a robust identification of
171 responsive neurons and, together with our choice of experimental conditions, optimized the
172 determination of CV.

173 *Intra- and interlaminar conduction velocity*

174 As an action potential propagates along the axon of an excitatory neuron, PV
175 interneurons closer to the site of initiation respond first and those farther away respond later (Fig.
176 4A). A sequence of frames taken at one msec intervals from 2 msec to 6 msec after stimulation
177 illustrate the spatiotemporal pattern of response spread (Fig. 4B). Note that these frames
178 represent the SNR at successive time points, compared to the maps in Figs. 1-3 showing the
179 maximum value within the entire post-stimulus measure window. The frames in Fig. 4B show
180 that PV interneuron responses occur first mostly nearer the stimulating electrode in L4 (2-3
181 msec), spread vertically both ways to L2/3 and L5 (4-5 msec), and then spread both vertically
182 and horizontally through L2/3 and L5 (5-6 msec). Thus, a single experiment can capture
183 propagation along different populations of axons, and because fields of view contained large
184 numbers of responsive neurons (typically \sim 50-100), we were generally able to identify 8 or more
185 neurons along distinct trajectories to track propagation. Fig. 4C-D presents resting fluorescence

186 and maximum SNR maps, respectively, showing the locations of responsive cells along one
187 selected trajectory (L4 → L2/3 CV). A plot of latency versus distance fitted to a line gave us the
188 CV as inverse of the slope (Fig. 4E). By constructing plots along different trajectories, we
189 determined the CV of different subpopulations of axons that target PV interneurons. Focusing on
190 PV interneurons in the same layer as the stimulation electrode (between dashed lines in Fig. 4B-
191 D) provided a determination of intralaminar (horizontal) CV, and focusing on PV interneurons in
192 the same barrel column as the stimulating electrode (between dotted lines in Fig. 4B-D) provided
193 a determination of interlaminar (vertical) CV. Interlaminar CV often included an additional
194 neighboring barrel column. This is consistent with results from rat BC indicating that excitatory
195 axons tend to project within the same and/or neighboring columns but usually not to columns
196 beyond the nearest neighbor (Narayanan et al., 2015).

197 In 22 out of 59 slices, plots of latency versus distance had statistically significant
198 correlations. Among the remaining slices, negative correlations occurred only rarely (4 out of 59
199 slices). The highest CV we were able to measure was 241 $\mu\text{m}/\text{msec}$ (19 PV interneurons), and
200 nearly half (15) of the experiments without significant positive correlations yielded CV values
201 above the highest measurable value. In these cases, the spread within the field of view was too
202 fast to detect differences in latency. In most cases of such rapid propagation, latencies varied by
203 less than 0.5 msec (average root-mean-square error = 0.427). These results indicate that in many
204 slices, the CV was faster than can be measured over the distances accessible within our field of
205 view. In the remainder of this work, we will focus primarily on CV measurements with
206 significant distance-latency correlations, unless stated otherwise, and recognize that this biases
207 our analysis uniformly toward slower conduction.



208 Stimulation in L2/3, L4, and L5 elicited responses that spread within those layers, and
 209 latency versus distance plots yielded intralaminar CV values in L2/3 and L5. In L4 the lack of
 210 correlation prevented us from determining the CV (N=3), and this may indicate that intralaminar

211 conduction is faster in this layer. L2/3 intralaminar CV measurements were generally slow with
212 low variance ($44 \pm 15 \mu\text{m}/\text{msec}$, $N = 52$ PV interneurons from 4 slices). The two measured L5
213 intralaminar CV values were very different ($28 \mu\text{m}/\text{msec}$ and $136 \mu\text{m}/\text{msec}$, $N = 18$ PV
214 interneurons from 2 slices), potentially reflecting differences between L5 pyramidal cell
215 subtypes, which are known to vary in target projection layers and morphology (Larsen &
216 Callaway, 2006). Fig. 5A shows a plot of latency versus distance with an intralaminar CV in
217 L2/3 of $37 \mu\text{m}/\text{msec}$ ($t = 4.86$, $p = 0.0009$).

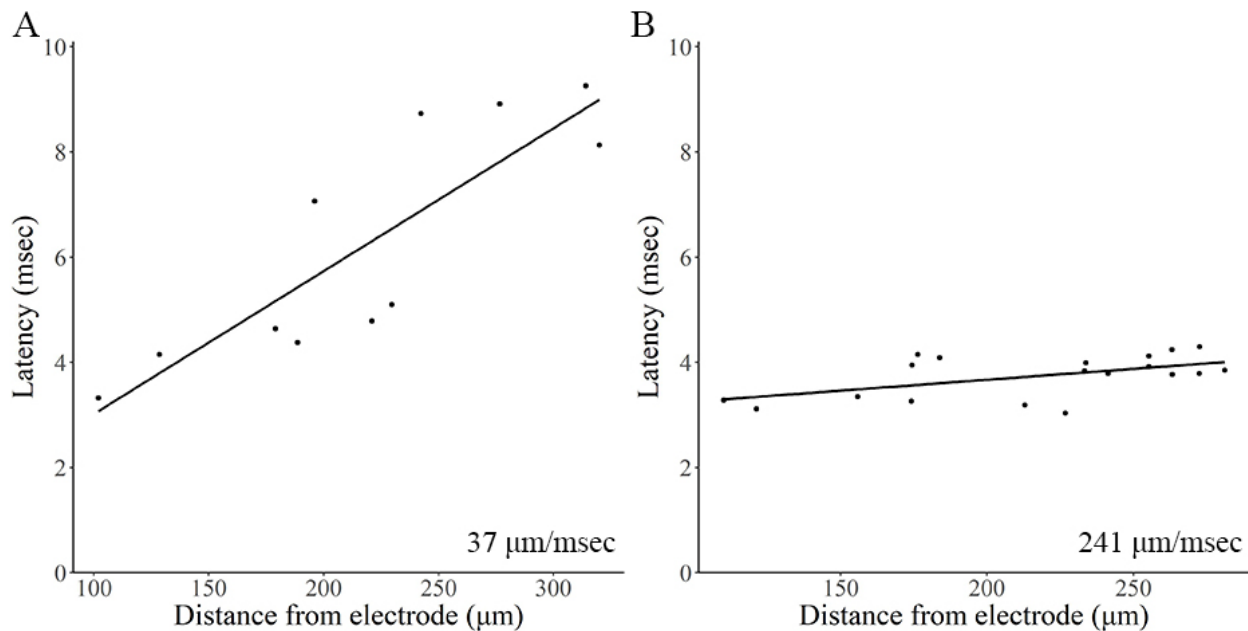


Figure 5. Latency versus intralaminar (A) or interlaminar (B) distance for two representative experiments. The steeper slope in A compared to B indicates that the L2/3 intralaminar CV represented in A ($37 \mu\text{m}/\text{msec}$) is slower than the L5 \rightarrow L4 interlaminar CV shown in B ($241 \mu\text{m}/\text{msec}$).

218 Correlated latency-distance plots for interlaminar propagation were obtained for all pairs
219 of layers with the exception of L5 \rightarrow L2/3. Fig. 5B shows a plot for L5 \rightarrow L4 conduction
220 yielding a CV of $241 \mu\text{m}/\text{msec}$ ($t = 2.63$, $p = 0.018$). For three other pairs of layers CV values
221 were similar to one another, with L4 \rightarrow L2/3 giving $\text{CV} = 94 \pm 37 \mu\text{m}/\text{msec}$ ($N = 62$ PV
222 interneurons, 3 slices), L5 \rightarrow L2/3 giving $\text{CV} = 107 \pm 48 \mu\text{m}/\text{msec}$ ($N = 57$ PV interneurons, 3
223 slices), and L2/3 \rightarrow L4 giving $\text{CV} = 81 \pm 36 \mu\text{m}/\text{msec}$ ($N = 93$ PV interneurons, 5 slices). Faster

224 CV values were obtained for L4 → L5 (144 $\mu\text{m}/\text{msec}$, N = 8 PV interneurons, 1 slice) and L5 →
225 L4 (154 \pm 58 $\mu\text{m}/\text{msec}$, N = 63 PV interneurons, 4 slices), including our fastest CV of 241
226 $\mu\text{m}/\text{msec}$ (Fig. 5B). The plot of latency versus distance for L5 → L4 in Fig. 5B is noticeably less
227 steep than the plot of L2/3 intralaminar CV in Fig. 5A, supporting the view that the L5 → L4 CV
228 is faster than the intralaminar CV.

229 Interlaminar CVs (111 \pm 49 $\mu\text{m}/\text{msec}$, N = 16 slices) were about twice as fast as
230 intralaminar CVs (57 \pm 41 $\mu\text{m}/\text{msec}$, N = 6 slices), and this difference was statistically
231 significant ($t = -2.587$, $p = 0.026$, Fig. 6A). This difference remained significant even excluding
232 the single particularly fast interlaminar CV value of 241 $\mu\text{m}/\text{msec}$ ($t = -2.352$, $p = 0.046$).
233 ANOVA followed by post-hoc testing revealed that intralaminar CV is about 2.7 times slower
234 than L5 → L4 interlaminar CV (Fig. 6B, ANOVA: $F = 3.085$, $p = 0.046$; Tukey's honestly
235 significant differences: L5 → L4 CV versus intralaminar CV: $p = 0.025$). Including values for
236 slices with CVs too fast to produce significant correlations further supports the assertion that
237 interlaminar CV is faster than intralaminar CV. This increased the number of intralaminar CV
238 measurements by 50% (N = 3 additional slices) but increased the number of interlaminar CV
239 measurements by 75% (N = 12 additional slices). Interestingly, one of these three additional
240 intralaminar CV values was from L4, possibly suggesting faster intralaminar CV in L4 than L2/3
241 or L5. Because a higher proportion of interlaminar CV values were too fast to measure, our focus
242 on experiments with statistically significant correlations underestimates the difference between
243 interlaminar and intralaminar CV.

244

245

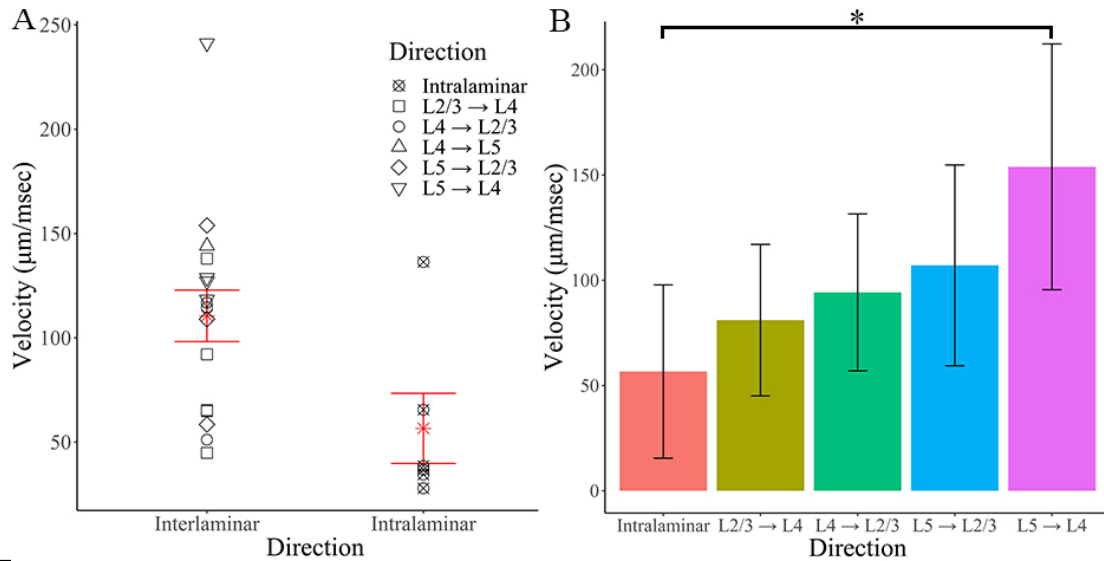


Figure 6. Inter- and intralaminar CV. A. Interlaminar CV ($111 \pm 49 \mu\text{m/msec}$) is approximately twice as fast as intralaminar CV ($57 \pm 41 \mu\text{m/msec}$; $t = -2.587$, $p = 0.026$). Symbol shapes indicate CV direction (in legend), and group mean \pm SD are shown in red. B. Intralaminar (70 PV interneurons, 6 slices), L2/3 \rightarrow L4 (93 PV interneurons, 5 slices), L4 \rightarrow L2/3 (62 PV interneurons, 3 slices), L5 \rightarrow L2/3 (57 PV interneurons, 3 slices), and L5 \rightarrow L4 (63 PV interneurons, 4 slices) CV. Error bars indicate SD. CV varies significantly based on direction ($F = 3.085$, $p = 0.046$), and intralaminar CV is significantly slower than L5 \rightarrow L4 CV ($p = 0.025$).

246 Discussion

247 Action potential conduction influences virtually all aspects of neural circuit function, and
248 many approaches have been taken to measure its velocity. Antidromic activation (Chomiak et al.,
249 2008; Palmer & Stuart, 2006; Salami, Itami, et al., 2003; Shlosberg et al., 2008), whole-cell
250 recording (Chomiak et al., 2008; Helmstaedter, Staiger, Sakmann, & Feldmeyer, 2008; Kim,
251 Renden, & von Gersdorff, 2013; Kimura et al., 2010; McDougall et al., 2018; Salami, Itami, et
252 al., 2003; Salami, Kimura, & Tsumoto, 2003; Shlosberg et al., 2008; Shu, Duque, Yu, Haider, &
253 McCormick, 2007) and voltage-sensitive dye imaging (Grinvald et al., 1981; Hamada et al.,
254 2017; Popovic et al., 2011; Sakai et al., 1991) provide accurate measurements of CV but are
255 limited by their low-throughput and lack of specificity. Other methods lack spatial resolution and
256 are poorly suited to investigations of single-cell responses (Candy & Szatkowski, 2000;
257 Drakesmith et al., 2019; Emmenegger, Obien, Franke, & Hierlemann, 2019; Kress & Mennerick,
258 2009; Radivojevic et al., 2017; Salami, Kimura, et al., 2003). The present study used the

259 genetically-encoded voltage sensor hVOS to measure CV of excitatory axons targeting PV
260 interneurons in mouse BC. Because it can be genetically targeted, hVOS provides a unique
261 opportunity to measure CV along axons innervating specific cell types. hVOS imaging has a
262 rapid response time that is well-suited for measuring the sub-millisecond differences in latency
263 required for the determination of CV. Although DPA increases membrane capacitance and thus
264 slows propagation, this effect is small as increasing DPA from 2 to 4 μM reduced CV by only
265 15% in mossy fibers (Ma et al., 2017). Furthermore, this uniform effect will reduce CV
266 proportionally in different populations of axons. In the present study it was difficult to measure
267 faster CV values, but this could be remedied by reducing magnification to track conduction over
268 longer distances. Our analysis has incorporated the assumption that axons follow a direct path to
269 target PV interneurons at different distances. This adds to the biases that reduce our estimates of
270 CV. This is probably more important for interlaminar than intralaminar conduction, as
271 interlaminar axons sometimes extend vertically through cortical layers before branching
272 horizontally (Larsen & Callaway, 2006; Schubert, Kotter, Luhmann, & Staiger, 2006).

273 CV values reported here are somewhat slower than in previous studies, which can
274 probably be attributed to our exclusion of experiments without a significant correlation between
275 latency and distance. Including these experiments yielded a value of $304 \pm 501 \mu\text{m}/\text{msec}$ ($N =$
276 670 PV interneurons from 37 slices), which trends toward the higher end of the range from
277 previous reports. Prior studies reported CV values of 140-160 $\mu\text{m}/\text{msec}$ in mouse anterior
278 cingulate cortex (Lee, Miao, Chen, Li, & Zhuo, 2021), 150-550 $\mu\text{m}/\text{msec}$ in rat visual cortex
279 (Murakoshi, Guo, & Ichinose, 1993), 161-240 $\mu\text{m}/\text{msec}$ in rat CA3 (Soleng, Raastad, &
280 Andersen, 2003), about 200-300 $\mu\text{m}/\text{msec}$ in mouse BC (Shlosberg et al., 2008), 200 $\mu\text{m}/\text{msec}$ in
281 rat BC (Helmstaedter et al., 2008), and 340 $\mu\text{m}/\text{msec}$ in rat primary somatosensory cortex

282 (Telfeian & Connors, 2003). While some of the variations in these studies can be attributed to
283 methodological differences such as temperature, this wide range of CV values probably also
284 reflects the diversity of cortical axons. Axonal diameter, varicosity geometry, and myelination
285 vary widely and all have a major impact on CV. Ion channel expression also varies widely
286 between cell types and compartments (Liu, Wang, Pitt, & Liu, 2022; Vacher, Mohapatra, &
287 Trimmer, 2008), and by controlling the intrinsic excitability of the axonal membrane will have
288 an impact on CV. Our measurements of CV values for different projections in the same
289 preparation offer a perspective to the variations between prior reports, and support the view that
290 this quantity can vary between axons in the same brain region.

291 PV interneuron microcircuitry, density, and excitation/inhibition input ratios differ
292 between cortical layers (Adesnik, 2018; Staiger & Petersen, 2021; Xu et al., 2016), and the CV
293 of axons innervating different PV interneurons will impact their function in cortical
294 microcircuits. The canonical cortical circuit for information flow begins with thalamic inputs to
295 L4 followed by transmission to L2/3 and then L5. We could follow this flow to measure a CV of
296 94 ± 37 $\mu\text{m}/\text{msec}$ along L4 excitatory axons targeting L2/3 PV interneurons. We also report CV
297 along excitatory axons following noncanonical circuits. For example, L2/3 receives input from
298 L5 (Narayanan et al., 2015; Staiger & Petersen, 2021; Thomson, West, Wang, & Bannister,
299 2002; Vecchia et al., 2020), and for this projection we measured a CV of 107 ± 48 $\mu\text{m}/\text{msec}$,
300 which was similar to the L4 \rightarrow L2/3 CV. We also measured CV along axons from L2/3 and L5
301 to L4 PV interneurons. Although most L2/3 excitatory cells project to infragranular or
302 supragranular cortical layers, a small portion target L4 PV interneurons (Thomson et al., 2002),
303 including a subset of L2/3 pyramidal cells with somata near the L3/4 border (Larsen & Callaway,
304 2006). Our L2/3 \rightarrow L4 CV of 81 ± 36 $\mu\text{m}/\text{msec}$ was slightly slower than other interlaminar CVs.

305 There is also evidence for monosynaptic L5 excitatory cell coupling to L4 fast-spiking
306 interneurons (Vecchia et al., 2020), and our CV in this direction of $154 \pm 58 \mu\text{m}/\text{msec}$ was
307 particularly rapid. These non-canonical pathways targeting L4 PV interneurons may influence
308 feedback to L4 and therefore impact integration of intracortical and incoming ventral
309 posteromedial thalamic input. Intralaminar spread was observed in L2/3, L4, and L5. The very
310 slow L2/3 intralaminar CV value reported here of $44 \pm 15 \mu\text{m}/\text{msec}$ is consistent with reported
311 values of 33-60 $\mu\text{m}/\text{msec}$ for intralaminar spread of population excitatory responses in this layer
312 (Petersen, Grinvald, & Sakmann, 2003).

313 Interestingly, we found the average intralaminar CV (of L2/3 and L5) to be about twice
314 as slow as the average interlaminar CV (Fig. 6A) and approximately 2.7 times slower than the
315 interlaminar L5 \rightarrow L4 CV (Fig. 6B). These differences have important implications for cortical
316 function. Long, horizontal L2/3 pyramidal cell axons have been previously observed in multiple
317 cortical areas across species (Bruno, Hahn, Wallace, de Kock, & Sakmann, 2009; Gilbert, 1992;
318 Gottlieb & Keller, 1997; Keller & Asanuma, 1993; McGuire, Gilbert, Rivlin, & Wiesel, 1991).
319 These projections are thought to connect cortical areas with similar functions, such as visual
320 regions with similar orientation selectivity (Gilbert, 1992). In BC, L2/3 pyramidal cell
321 intralaminar axons tend to extend across barrels corresponding to whisker rows rather than arcs,
322 possibly reflecting a directional preference (Feldmeyer, 2012). Both regular-spiking and fast-
323 spiking units, putative pyramidal cells and PV interneurons, respectively, show selectivity to
324 whisking direction in BC L2/3 (Andermann & Moore, 2006; Kremer, Leger, Goodman, Brette,
325 & Bourdieu, 2011). Our measurement of L2/3 intralaminar CV may reflect the targeting of the
326 PV interneurons of these domains. Murine L5 intralaminar excitatory projections connect
327 multiple barrel columns (Schubert et al., 2006; Schubert et al., 2001), and intralaminar excitatory

328 inputs to L5 pyramidal cells usually extend across one and a half barrel columns, so L5
329 pyramidal cells may integrate information from three whiskers. Thus, the L5 intralaminar CV is
330 likely to impact multi-whisker integration. While L5 → L4 axonal projections are uncommon
331 (Staiger & Petersen, 2021), optogenetic stimulation of L5 pyramidal cells elicits firing in L4 fast-
332 spiking interneurons, and inhibition of L5 pyramidal cells lengthens the reaction time in a texture
333 discrimination test (Vecchia et al., 2020). L5 → L4 CV may therefore impact temporal sharpness
334 of responses to sensory stimuli. Together, these results suggest that interlaminar cortical circuits
335 process more rapidly than intralaminar circuits. Thus, precise timing of inputs to PV interneurons
336 is likely to play an important role in computations performed within a cortical column and to be
337 less critical in the collective computations performed by multiple columns. The higher CV for
338 interlaminar conduction than intralaminar conduction found in the present study will thus meet
339 distinct demands of different forms of cortical computation.

340 hVOS imaging offers a new and powerful approach to the study of CV, not only in the
341 axons of defined cell types (Ma et al., 2017), but also in the axons defined by their targeted cell
342 types. An important example of such specificity is that thalamocortical projections to inhibitory
343 neurons have a faster CV than projections to excitatory cells, allowing interlaminar inhibition to
344 activate L4 targets prior to L2/3 targets (Kimura et al., 2010). Targeting hVOS probes to
345 different types of neurons has the potential to reveal many additional forms of axon
346 specialization adapted to different forms of neuronal computation.

347

348 **Materials and Methods**

349 *Animals*

350 Ai35-hVOS1.5 (C57BL/6-*Gt(ROSA)26Sor^{tm1(CAG-hVOS1.5)Mbj}*/J, JAX 031102) Cre reporter
351 mice (Bayguinov et al., 2017) were bred with PV Cre driver mice (B6.129P2-Pvalb^{tm1(cre)Arbr}/J,
352 JAX 017320) to create animals with PV interneuron-specific hVOS probe expression. All animal
353 procedures were approved by the Animal Care and Use Committee of the University of
354 Wisconsin-Madison School of Medicine and Public Health (ACUC protocol: M005952).

355 *Hybrid voltage sensor (hVOS)*

356 The hVOS probe used here harbors a cerulean fluorescent protein (CeFP) tethered to the
357 inner cell membrane by a truncated h-ras motif (Wang, Zhang, Chanda, & Jackson, 2010). Slices
358 are perfused with 4 μ M dipicrylamine (DPA), a small anion which partitions into the cell
359 membrane. Membrane depolarization drives DPA towards the CeFP to quench fluorescence
360 through Förster resonance energy transfer. Repolarization drives the DPA away allowing
361 fluorescence to return to baseline (Chanda et al., 2005; Wang et al., 2010). Fluorescence thus
362 reports voltage changes selectively from PV interneurons because these cells express the probe
363 with very high specificity (Bayguinov et al., 2017). DPA has a time resolution < 0.5 msec
364 (Bradley, Luo, Otis, & DiGregorio, 2009; Chanda et al., 2005) and tracks action potentials with
365 excellent temporal fidelity (Ghitani et al., 2015; Ma et al., 2019). Parameters such as latency,
366 amplitude, and half-width were determined from traces of fluorescence versus time (Fig. 7).
367 Amplitude was taken as the peak change in fluorescence from the pre-stimulus baseline, and
368 half-width as the time between rise and fall at half-maximal response. Latency is the time from
369 stimulation to half-maximal response.

370 *Slice preparation*

371 Four- to ten-week-old male and female mice were deeply anesthetized with isoflurane
372 and sacrificed via cervical dislocation. Brains were dissected and placed into ice-cold cutting
373 solution (in mM: 10 glucose, 125 NaCl, 4 KCl, 1.25 NaH₂PO₄, 26 NaHCO₃, 6 MgSO₄, 1 CaCl₂)
374 bubbled with 95% O₂/5% CO₂. Coronal slices (300 μ m) were prepared using a Leica VT1200S
375 vibratome and placed into artificial cerebrospinal fluid (ACSF, same as cutting solution except
376 1.3 mM MgSO₄, 2.5 mM CaCl₂, and 4 μ M DPA) and bubbled with 95% O₂/5% CO₂ for at least
377 one hour.

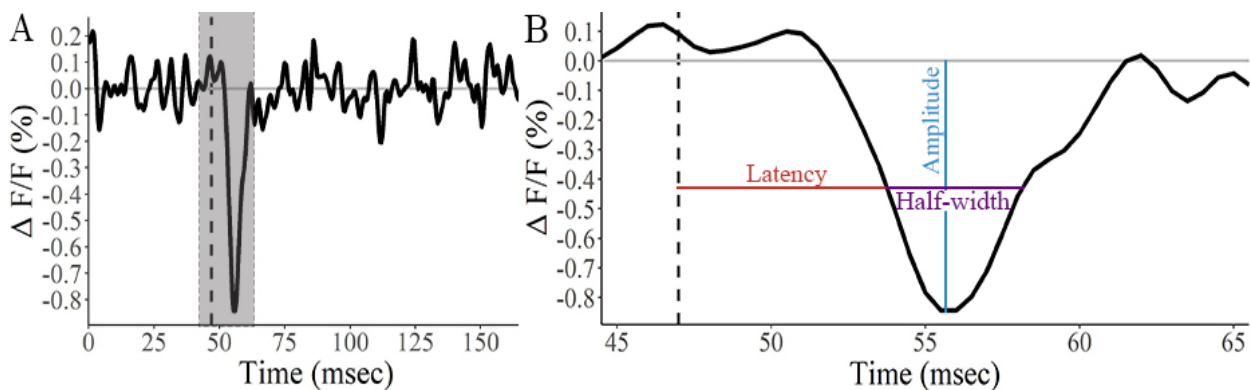


Figure 7. PV interneuron electrical activity was recorded as fluorescence using a genetically-encoded hybrid voltage sensor (hVOS). A. PV interneuron response parameters are extracted from traces of fluorescence versus time. Gray shading indicates the 20 msec measurement window expanded in B. B. Amplitude is the maximum change in fluorescence from baseline. Half-width is the time between half-maximal change in fluorescence during the rising and decay phases. Latency is the time from stimulation to half-maximal change in fluorescence of the rising phase.

378 *Voltage imaging*

379 Slices were continuously perfused with ACSF at room temperature and viewed using a
380 BX51 Olympus microscope. Layer and barrel boundaries were visually identified based on both
381 fluorescence and gradient contrast images (Feldmeyer, 2012; Woolsey & Van der Loos, 1970).
382 Stimulus pulses (100 μ A, 180- μ sec, except Fig. 2A-C which used 10-60 μ A) were generated by a
383 stimulus isolator (World Precision Instruments, Sarasota, Florida) and applied to various
384 locations within BC with fire-polished, ACSF-filled KG-33 glass electrodes (King Precision
385 Glass, Claremont, California) with tip diameter \sim 6-8 μ m. Traces of fluorescence versus time
386 were averages of 15-30 trials. Slices were illuminated with 435 nm light using an LED light

387 source (Prizmatix, Holon, Israel). Gradient contrast images were acquired with a Kiralux
388 (Thorlabs, Newton, New Jersey) CMOS camera; fluorescent images were acquired with this
389 camera for better visualization, but for voltage imaging we used a CCD-SMQ camera (RedShirt
390 Imaging, Decatur, Georgia) at a framerate of 2000 Hz and 80x80 spatial resolution. Data were
391 acquired with a custom data acquisition and analysis program that controlled stimulation and
392 illumination (Chang, 2006).

393 *Data processing and analysis*

394 Fluorescence divided by resting light intensity ($\Delta F/F$) was passed through a nine-point
395 binomial temporal filter and a spatial filter with $\sigma = 1$. A polynomial baseline correction was
396 calculated using fluorescence outside of a 20 msec measurement window from 2 msec before to
397 18 msec after the stimulus. Parameters including amplitude, half-width, and latency were
398 calculated from traces of fluorescence versus time. Heatmaps showing SNR are each normalized
399 to the maximum value within the field of view (with the exception of Fig. 2A-D, as explained in
400 the figure legend). Heatmaps showing maximum amplitude and associated traces of fluorescence
401 over time (Fig. 1) are normalized but not divided by resting light intensity.

402 *Responsive neuron identification*

403 We developed a semi-automated method for objective, reproducible identification of
404 responsive PV interneurons. Supp. Fig. 1 is an extension of Fig. 3 and illustrates this process.
405 The peak fluorescence change from baseline in the 20 msec post-stimulus time window (Fig. 7B)
406 was calculated for each pixel and divided by the pre-stimulus root-mean-square fluorescence
407 during a 20 msec pre-stimulus interval to give the SNR. A SNR cutoff was determined using the
408 pre-stimulus root-mean-square values, and pixels with a response SNR < cutoff were discarded
409 (gray pixels, Supp. Fig. 1A). k-means clustering was then performed on the SNR of the

410 remaining pixels (Supp. Fig. 1B). This served two main purposes. First, k-means clustering
411 divides pixels into groups likely to contain responsive cells, using the criterion that only pixels
412 with $\text{SNR} > 5$ represent responsive cell bodies (corresponding to yellow, light blue, and medium
413 blue clusters, Supp. Fig. 1B). Second, if multiple pixels represent one cell body, they are likely to
414 have similar SNR values. Because each k-means cluster contains pixels with similar SNRs, two
415 pixels in the same cluster sharing a face are likely to represent the same cell body. This method
416 basically compared each pixel to its neighbors and grouped them based on the likelihood they
417 represent the same cell. One or more contiguous pixels in the same SNR cluster were grouped as
418 one cell if they were no greater than three pixels across, because each pixel measures $6.68 \mu\text{m}$,
419 and murine PV interneuron somata are approximately $20 \mu\text{m}$ in diameter (Kooijmans et al.,
420 2020; Selby et al., 2007; Y. Wang et al., 2002). These criteria excluded some larger clusters of
421 pixels as potentially representing more than one cell even though they had a high SNR. For
422 example, some yellow and orange pixels in Fig. 3C and Supp. Fig. 1A, which correspond with
423 the highest SNR k-means cluster (yellow) in Supp. Fig. 1B, form groups which are larger than 3
424 pixels across and therefore must contain more than one cell. Likewise, Fig. 2D had fewer
425 identifiable responsive cells than Fig. 2C because Fig. 2D had greater overlap. Pixel groups with
426 $\text{SNR} < 5$ or amplitude < 0.001 were excluded and not used to select individual responsive
427 neurons. We also excluded groups of pixels sharing a face to ensure that a single group did not
428 represent multiple cells. The rationale for this grouping procedure is that pixels draw from an
429 area that is smaller than a PV interneuron cell body, and we expect SNR to be uniform over the
430 soma of one neuron. Pixels at a cell edge will not be included due to their lower SNR. Thus, this
431 criterion is conservative in focusing on pixels containing signals arising from distinct, spatially
432 separated neurons.

433 *Experimental design and statistical tests*

434 Further analysis of responses from groups of pixels identified as described above was
435 performed using R and Python. Responses with latency < 1 msec were removed to exclude the
436 effect of direct stimulation; these were generally very close to the stimulation electrode.
437 Responses with latency or time to peak > 13 msec were removed to exclude polysynaptic
438 responses. Disynaptic responses, defined as those occurring more than 2 msec after responses
439 from neighboring cells ($< \sim 20 \mu\text{m}$) were also excluded. Potential outliers, defined as responses
440 with amplitude, half-width, or latency outside the first or third quartile $\pm 1.5 * \text{interquartile}$
441 range, were iteratively identified and visually verified or excluded as appropriate.

442 Each CV was based on a plot of latency versus distance with at least 8 responsive cells \geq
443 $100 \mu\text{m}$ from the stimulating electrode, spanning a range of distances $\geq 100 \mu\text{m}$. Analyses
444 included 855 PV interneurons from 59 slices from 13 animals (6 female and 7 male).
445 Relationships between latency and distance were evaluated with linear regression, and p-values
446 were corrected for multiple tests using the false-discovery rate. Euclidean distance was
447 determined between pixels on the 80×80 grid of the CCD-SMQ camera. To determine the
448 appropriate statistical tests, normality was evaluated with a Shapiro-Wilk test, and differences in
449 group variances were evaluated with Levene's tests. CV was normally distributed ($W = 0.9115$,
450 $p = 0.051$). Variance did not differ significantly for male and female animals ($F = 1.2505$, $p =$
451 0.277), for inter- and intralaminar CV ($F = 0.516$, $p = 0.481$), or for CV directions (intralaminar,
452 $L2/3 \rightarrow L4$, $L4 \rightarrow L2/3$, $L5 \rightarrow L2/3$, $L5 \rightarrow L4$; $F = 0.0519$, $p = 0.994$). Therefore, interlaminar
453 versus intralaminar CV, and CV for male versus female animals were compared with t-tests. CV
454 did not differ significantly based on sex ($t = 0.289$, $p = 0.778$). The effect of direction on CV was

455 evaluated with ANOVA followed by post-hoc comparisons using Tukey's honestly significant
456 differences.

457 *Code accessibility*

458 Custom software, R code, and Python code available on request.

459 **References**

- 460 Adesnik, H. (2018). Layer-specific excitation/inhibition balances during neuronal synchronization in the
461 visual cortex. *J Physiol*, 596(9), 1639-1657. doi:10.1113/JP274986
- 462 Andermann, M. L., & Moore, C. I. (2006). A somatotopic map of vibrissa motion direction within a
463 barrel column. *Nat Neurosci*, 9(4), 543-551. doi:10.1038/n1671
- 464 Bayguinov, P. O., Ma, Y., Gao, Y., Zhao, X., & Jackson, M. B. (2017). Imaging Voltage in Genetically
465 Defined Neuronal Subpopulations with a Cre Recombinase-Targeted Hybrid Voltage Sensor. *J*
466 *Neurosci*, 37(38), 9305-9319. doi:10.1523/JNEUROSCI.1363-17.2017
- 467 Bradley, J., Luo, R., Otis, T. S., & DiGregorio, D. A. (2009). Submillisecond optical reporting of
468 membrane potential in situ using a neuronal tracer dye. *J Neurosci*, 29(29), 9197-9209.
469 doi:10.1523/JNEUROSCI.1240-09.2009
- 470 Bruno, R. M., Hahn, T. T., Wallace, D. J., de Kock, C. P., & Sakmann, B. (2009). Sensory experience
471 alters specific branches of individual corticocortical axons during development. *J Neurosci*,
472 29(10), 3172-3181. doi:10.1523/JNEUROSCI.5911-08.2009
- 473 Bucher, D., & Goaillard, J. M. (2011). Beyond faithful conduction: short-term dynamics,
474 neuromodulation, and long-term regulation of spike propagation in the axon. *Prog Neurobiol*,
475 94(4), 307-346. doi:10.1016/j.pneurobio.2011.06.001
- 476 Candy, S. M., & Szatkowski, M. S. (2000). Neuronal excitability and conduction velocity changes in
477 hippocampal slices from streptozotocin-treated diabetic rats. *Brain Res*, 863, 298-301.
478 doi:10.1016/s0006-8993(00)02171-5
- 479 Cardin, J. A. (2018). Inhibitory Interneurons Regulate Temporal Precision and Correlations in Cortical
480 Circuits. *Trends Neurosci*, 41(10), 689-700. doi:10.1016/j.tins.2018.07.015
- 481 Chanda, B., Blunck, R., Faria, L. C., Schweizer, F. E., Mody, I., & Bezanilla, F. (2005). A hybrid
482 approach to measuring electrical activity in genetically specified neurons. *Nat Neurosci*, 8(11),
483 1619-1626. doi:10.1038/n1558
- 484 Chang, P.-P. (2006). *Heterogeneous spatial patterns of long-term potentiation in hippocampal slices*.
485 University of Wisconsin-Madison, Madison.
- 486 Chomiak, T., Peters, S., & Hu, B. (2008). Functional architecture and spike timing properties of
487 corticofugal projections from rat ventral temporal cortex. *J Neurophysiol*, 100(1), 327-335.
488 doi:10.1152/jn.90392.2008
- 489 Compston, A., & Coles, A. (2002). Multiple Sclerosis. *Lancet*, 359, 1221-1231. doi:10.1016/S0140-
490 6736(02)08220-X
- 491 Corcoba, A., Steullet, P., Duarte, J. M., Van de Looij, Y., Monin, A., Cuenod, M., Gruetter, R., & Do, K.
492 Q. (2015). Glutathione Deficit Affects the Integrity and Function of the Fimbria/Fornix and
493 Anterior Commissure in Mice: Relevance for Schizophrenia. *Int J Neuropsychopharmacol*, 19(3),
494 pyv110. doi:10.1093/ijnp/pyv110
- 495 Drakesmith, M., Harms, R., Rudrapatna, S. U., Parker, G. D., Evans, C. J., & Jones, D. K. (2019).
496 Estimating axon conduction velocity in vivo from microstructural MRI. *Neuroimage*, 203,
497 116186. doi:10.1016/j.neuroimage.2019.116186

- 498 Emmenegger, V., Obien, M. E. J., Franke, F., & Hierlemann, A. (2019). Technologies to Study Action
499 Potential Propagation With a Focus on HD-MEAs. *Front Cell Neurosci*, *13*, 159.
500 doi:10.3389/fncel.2019.00159
- 501 Feldmeyer, D. (2012). Excitatory neuronal connectivity in the barrel cortex. *Front Neuroanat*, *6*, 24.
502 doi:10.3389/fnana.2012.00024
- 503 Ferguson, B. R., & Gao, W. J. (2018). PV Interneurons: Critical Regulators of E/I Balance for Prefrontal
504 Cortex-Dependent Behavior and Psychiatric Disorders. *Front Neural Circuits*, *12*, 37.
505 doi:10.3389/fncir.2018.00037
- 506 Fields, R. D. (2015). A new mechanism of nervous system plasticity: activity-dependent myelination. *Nat*
507 *Rev Neurosci*, *16*(12), 756-767. doi:10.1038/nrn4023
- 508 Fukuda, T., & Kosaka, T. (2003). Ultrastructural study of gap junctions between dendrites of
509 parvalbumin-containing GABAergic neurons in various neocortical areas of the adult rat.
510 *Neuroscience*, *120*(1), 5-20. doi:10.1016/s0306-4522(03)00328-2
- 511 Galarreta, M., & Hestrin, S. (2002). Electrical and chemical synapses among parvalbumin fast-spiking
512 GABAergic interneurons in adult mouse neocortex. *PNAS*, *99*, 12438-12443.
513 doi:10.1073/pnas.192159599
- 514 Gandal, M. J., Edgar, J. C., Klook, K., & Siegel, S. J. (2012). Gamma synchrony: towards a translational
515 biomarker for the treatment-resistant symptoms of schizophrenia. *Neuropharmacology*, *62*(3),
516 1504-1518. doi:10.1016/j.neuropharm.2011.02.007
- 517 Ghitani, N., Bayguinov, P. O., Ma, Y., & Jackson, M. B. (2015). Single-trial imaging of spikes and
518 synaptic potentials in single neurons in brain slices with genetically encoded hybrid voltage
519 sensor. *J Neurophysiol*, *113*(4), 1249-1259. doi:10.1152/jn.00691.2014
- 520 Gilbert, C. D. (1992). Horizontal Integration and Cortical Dynamics. *Neuron*, *9*, 1-13. doi:10.1016/0896-
521 6273(92)90215-y
- 522 Gloveli, T., Dugladze, T., Saha, S., Monyer, H., Heinemann, U., Traub, R. D., Whittington, M. A., &
523 Buhl, E. H. (2005). Differential involvement of oriens/pyramidal interneurons in hippocampal
524 network oscillations in vitro. *J Physiol*, *562*(Pt 1), 131-147. doi:10.1113/jphysiol.2004.073007
- 525 Gonzalez-Burgos, G., Cho, R. Y., & Lewis, D. A. (2015). Alterations in cortical network oscillations and
526 parvalbumin neurons in schizophrenia. *Biol Psychiatry*, *77*(12), 1031-1040.
527 doi:10.1016/j.biopsych.2015.03.010
- 528 Gottlieb, J. P., & Keller, A. (1997). Intrinsic circuitry and physiological properties of pyramidal neurons
529 in rat barrel cortex. *Exp Brain Res*, *115*, 47-60. doi:10.1007/pl00005684
- 530 Grinvald, A., Ross, W. N., & Farber, I. (1981). Simultaneous optical measurements of electrical activity
531 from multiple sites on processes of cultured neurons. *Proc Natl Acad Sci U S A*, *78*.
532 doi:10.1073/pnas.78.5.3245
- 533 Hamada, M. S., Popovic, M. A., & Kole, M. H. (2017). Loss of Saltation and Presynaptic Action
534 Potential Failure in Demyelinated Axons. *Front Cell Neurosci*, *11*, 45.
535 doi:10.3389/fncel.2017.00045
- 536 Helmstaedter, M., Staiger, J. F., Sakmann, B., & Feldmeyer, D. (2008). Efficient recruitment of layer 2/3
537 interneurons by layer 4 input in single columns of rat somatosensory cortex. *J Neurosci*, *28*(33),
538 8273-8284. doi:10.1523/JNEUROSCI.5701-07.2008
- 539 Ivanov, V., Polykretis, I. F., & Michmizos, K. P. (2019). *Axonal Conduction Velocity Impacts Neuronal*
540 *Network Oscillations*. Paper presented at the 2019 IEEE EMBS International Conference on
541 Biomedical & Health Informatics (BHI).
- 542 Keller, A., & Asanuma, H. (1993). Synaptic Relationships Involving Local Axon Collaterals of Pyramidal
543 Neurons in Cat Motor Cortex. *J Comp Neurol*, *336*, 229-242. doi:10.1002/cne.903360206
- 544 Kim, J. H., Renden, R., & von Gersdorff, H. (2013). Dysmyelination of auditory afferent axons increases
545 the jitter of action potential timing during high-frequency firing. *J Neurosci*, *33*(22), 9402-9407.
546 doi:10.1523/JNEUROSCI.3389-12.2013
- 547 Kimura, F., Itami, C., Ikezoe, K., Tamura, H., Fujita, I., Yanagawa, Y., Obata, K., & Ohshima, M. (2010).
548 Fast activation of feedforward inhibitory neurons from thalamic input and its relevance to the

- 549 regulation of spike sequences in the barrel cortex. *J Physiol*, 588(Pt 15), 2769-2787.
550 doi:10.1113/jphysiol.2010.188177
- 551 Kooijmans, R. N., Sierhuis, W., Self, M. W., & Roelfsema, P. R. (2020). A Quantitative Comparison of
552 Inhibitory Interneuron Size and Distribution between Mouse and Macaque V1, Using Calcium-
553 Binding Proteins. *Cereb Cortex Commun*, 1(1), tgaa068. doi:10.1093/texcom/tgaa068
- 554 Kremer, Y., Leger, J. F., Goodman, D., Brette, R., & Bourdieu, L. (2011). Late emergence of the vibrissa
555 direction selectivity map in the rat barrel cortex. *J Neurosci*, 31(29), 10689-10700.
556 doi:10.1523/JNEUROSCI.6541-10.2011
- 557 Kress, G. J., & Mennerick, S. (2009). Action potential initiation and propagation: upstream influences on
558 neurotransmission. *Neuroscience*, 158(1), 211-222. doi:10.1016/j.neuroscience.2008.03.021
- 559 Larsen, D. D., & Callaway, E. M. (2006). Development of layer-specific axonal arborizations in mouse
560 primary somatosensory cortex. *J Comp Neurol*, 494(3), 398-414. doi:10.1002/cne.20754
- 561 Lauber, E., Filice, F., & Schwaller, B. (2018). Parvalbumin neurons as a hub in autism spectrum
562 disorders. *J Neurosci Res*, 96(3), 360-361. doi:10.1002/jnr.24204
- 563 Lee, J. A., Miao, Z., Chen, Q. Y., Li, X. H., & Zhuo, M. (2021). Multiple synaptic connections into a
564 single cortical pyramidal cell or interneuron in the anterior cingulate cortex of adult mice. *Mol*
565 *Brain*, 14(1), 88. doi:10.1186/s13041-021-00793-8
- 566 Liu, Wang, H. G., Pitt, G. S., & Liu, Z. J. (2022). Direct Observation of Compartment-Specific
567 Localization and Dynamics of Voltage-Gated Sodium Channels. *J Neurosci*, 42(28), 5482-5498.
568 doi:10.1523/JNEUROSCI.0086-22.2022
- 569 Liu, T. Y., Hsieh, J. C., Chen, Y. S., Tu, P. C., Su, T. P., & Chen, L. F. (2012). Different patterns of
570 abnormal gamma oscillatory activity in unipolar and bipolar disorder patients during an implicit
571 emotion task. *Neuropsychologia*, 50(7), 1514-1520. doi:10.1016/j.neuropsychologia.2012.03.004
- 572 Ma, Y., Bayguinov, P. O., & Jackson, M. B. (2017). Action Potential Dynamics in Fine Axons Probed
573 with an Axonally Targeted Optical Voltage Sensor. *eNeuro*, 4(4), 0146-0147.
574 doi:10.1523/ENEURO.0146-17.2017
- 575 Ma, Y., Bayguinov, P. O., & Jackson, M. B. (2019). Optical Studies of Action Potential Dynamics with
576 hVOS probes. *Curr Opin Biomed Eng*, 12, 51-58. doi:10.1016/j.cobme.2019.09.007
- 577 McDougall, S., Vargas Riad, W., Silva-Gotay, A., Tavares, E. R., Harpalani, D., Li, G. L., & Richardson,
578 H. N. (2018). Myelination of Axons Corresponds with Faster Transmission Speed in the
579 Prefrontal Cortex of Developing Male Rats. *eNeuro*, 5(4), 0203-0218.
580 doi:10.1523/ENEURO.0203-18.2018
- 581 McGuire, B. A., Gilbert, C. D., Rivlin, P. K., & Wiesel, T. N. (1991). Targets of Horizontal Connections
582 in Macaque Primary Visual Cortex. *J Comp Neurol*, 305(3), 370-392.
583 doi:10.1002/cne.903050303
- 584 Murakoshi, T., Guo, J., & Ichinose, T. (1993). Electrophysiological identification of horizontal synaptic
585 connections in rat visual cortex in vitro. *Neurosci Lett*, 163(2), 211-214. doi:10.1016/0304-
586 3940(93)90385-x
- 587 Narayanan, R. T., Egger, R., Johnson, A. S., Mansvelder, H. D., Sakmann, B., de Kock, C. P., &
588 Oberlaender, M. (2015). Beyond Columnar Organization: Cell Type- and Target Layer-Specific
589 Principles of Horizontal Axon Projection Patterns in Rat Vibrissal Cortex. *Cereb Cortex*, 25(11),
590 4450-4468. doi:10.1093/cercor/bhv053
- 591 Nave, K. A. (2010). Myelination and support of axonal integrity by glia. *Nature*, 468(7321), 244-252.
592 doi:10.1038/nature09614
- 593 Olmos-Serrano, J. L., Kang, H. J., Tyler, W. A., Silbereis, J. C., Cheng, F., Zhu, Y., Pletikos, M.,
594 Jankovic-Rapan, L., Cramer, N. P., Galdzicki, Z., Goodliffe, J., Peters, A., Sethares, C., Delalle,
595 I., Golden, J. A., Haydar, T. F., & Sestan, N. (2016). Down Syndrome Developmental Brain
596 Transcriptome Reveals Defective Oligodendrocyte Differentiation and Myelination. *Neuron*,
597 89(6), 1208-1222. doi:10.1016/j.neuron.2016.01.042
- 598 Pajevic, S., Bassar, P. J., & Fields, R. D. (2014). Role of myelin plasticity in oscillations and synchrony
599 of neuronal activity. *Neuroscience*, 276, 135-147. doi:10.1016/j.neuroscience.2013.11.007

- 600 Palmer, L. M., & Stuart, G. J. (2006). Site of action potential initiation in layer 5 pyramidal neurons. *J*
601 *Neurosci*, 26(6), 1854-1863. doi:10.1523/JNEUROSCI.4812-05.2006
- 602 Panzera, L. C., & Hoppa, M. B. (2019). Genetically Encoded Voltage Indicators Are Illuminating
603 Subcellular Physiology of the Axon. *Front Cell Neurosci*, 13, 52. doi:10.3389/fncel.2019.00052
- 604 Pedroni, A., Minh do, D., Mallamaci, A., & Cherubini, E. (2014). Electrophysiological characterization of
605 granule cells in the dentate gyrus immediately after birth. *Front Cell Neurosci*, 8, 44.
606 doi:10.3389/fncel.2014.00044
- 607 Petersen, C. C. H., Grinvald, A., & Sakmann, B. (2003). Spatiotemporal Dynamics of Sensory Responses
608 in Layer 2/3 of Rat Barrel Cortex Measured In Vivo by Voltage-Sensitive Dye Imaging
609 Combined with Whole-Cell Voltage Recordings and Neuron Reconstructions. *J Neurosci*, 23(4),
610 1298-1309. doi:10.1523/JNEUROSCI.23-04-01298.2003
- 611 Popovic, M. A., Foust, A. J., McCormick, D. A., & Zecevic, D. (2011). The spatio-temporal
612 characteristics of action potential initiation in layer 5 pyramidal neurons: a voltage imaging study.
613 *J Physiol*, 589(17), 4167-4187. doi:10.1113/jphysiol.2011.209015
- 614 Pouille, F., & Scanziani, M. (2001). Enforcement of temporal fidelity in pyramidal cells by somatic feed-
615 forward inhibition. *Science*, 293(5532), 1159-1163. doi:10.1126/science.1060342
- 616 Radivojevic, M., Franke, F., Altermatt, M., Muller, J., Hierlemann, A., & Bakkum, D. J. (2017). Tracking
617 individual action potentials throughout mammalian axonal arbors. *Elife*, 6.
618 doi:10.7554/eLife.30198
- 619 Roy, K., Murtie, J. C., El-Khodor, B. F., Edgar, N., Sardi, S. P., Hooks, B. M., Benoit-Marand, M., Chen,
620 C., Moore, H., O'Donnell, P., Brunner, D., & Corfas, G. (2007). Loss of erbB signaling in
621 oligodendrocytes alters myelin and dopaminergic function, a potential mechanism for
622 neuropsychiatric disorders. *PNAS*, 104(19), 8131-8136. doi:10.1073/pnas.0702157104
- 623 Sakai, T., Komuro, H., Katoh, Y., Sasaki, H., Momose-Sato, Y., & Kamino, K. (1991). Optical
624 Determination of Impulsive Conduction Velocity During Development of Embryonic chick
625 Cervical Vagus Nerve Bundles. *J Physiol*, 439, 361-381. doi:10.1113/jphysiol.1991.sp018671
- 626 Salami, M., Itami, C., Tsumoto, T., & Kimura, F. (2003). Change of conduction velocity by regional
627 myelination yields constant latency irrespective of distance between thalamus and cortex. *PNAS*,
628 100(10), 6174-6179. doi:10.1073/pnas.0937380100
- 629 Salami, M., Kimura, F., & Tsumoto, T. (2003). Postnatal Changes of Conduction Velocity of the Fibers in
630 and out of the Mouse Barrel Cortex. *Iran Biomed J*, 7(2), 57-63.
- 631 Schubert, D., Kotter, R., Luhmann, H. J., & Staiger, J. F. (2006). Morphology, electrophysiology and
632 functional input connectivity of pyramidal neurons characterizes a genuine layer va in the
633 primary somatosensory cortex. *Cereb Cortex*, 16(2), 223-236. doi:10.1093/cercor/bhi100
- 634 Schubert, D., Staiger, J. F., Cho, N., Kotter, R., Zilles, K., & Luhmann, H. J. (2001). Layer-Specific
635 Intracolumnar and Transcolumnar Functional Connectivity of Layer V Pyramidal Cells in Rat
636 Barrel Cortex. *J Neurosci*, 21(10), 3580-3592. doi:10.1523/JNEUROSCI.21-10-03580.2001
- 637 Selby, L., Zhang, C., & Sun, Q. Q. (2007). Major defects in neocortical GABAergic inhibitory circuits in
638 mice lacking the fragile X mental retardation protein. *Neurosci Lett*, 412(3), 227-232.
639 doi:10.1016/j.neulet.2006.11.062
- 640 Shlosberg, D., Abu-Ghanem, Y., & Amitai, Y. (2008). Comparative properties of excitatory and
641 inhibitory inter-laminar neocortical axons. *Neuroscience*, 155(2), 366-373.
642 doi:10.1016/j.neuroscience.2008.06.003
- 643 Shu, Y., Duque, A., Yu, Y., Haider, B., & McCormick, D. A. (2007). Properties of action-potential
644 initiation in neocortical pyramidal cells: evidence from whole cell axon recordings. *J*
645 *Neurophysiol*, 97(1), 746-760. doi:10.1152/jn.00922.2006
- 646 Soleng, A. F., Raastad, M., & Andersen, P. (2003). Conduction latency along CA3 hippocampal axons
647 from rat. *Hippocampus*, 13(8), 953-961. doi:10.1002/hipo.10141
- 648 Staiger, J. F., & Petersen, C. C. H. (2021). Neuronal Circuits in Barrel Cortex for Whisker Sensory
649 Perception. *Physiol Rev*, 101(1), 353-415. doi:10.1152/physrev.00019.2019

- 650 Telfeian, A. E., & Connors, B. W. (2003). Widely integrative properties of layer 5 pyramidal cells support
651 a role for processing of extralaminar synaptic inputs in rat neocortex. *Neuroscience Letters*,
652 343(2), 121-124. doi:10.1016/s0304-3940(03)00379-3
- 653 Thomson, A. M., West, D. C., Wang, Y., & Bannister, A. P. (2002). Synaptic Connections and Small
654 Circuits Involving Excitatory and Inhibitory Neurons in Layers 2-5 of Adult Rat and Cat
655 Neocortex: Triple Intracellular Recordings and Biocytin Labelling In Vitro. *Cereb Cortex*, 12(9),
656 936-953. doi:10.1093/cercor/12.9.936
- 657 Vacher, H., Mohapatra, D. P., & Trimmer, J. S. (2008). Localization and targeting of voltage-dependent
658 ion channels in mammalian central neurons. *Physiol Rev*, 88(4), 1407-1447.
659 doi:10.1152/physrev.00002.2008
- 660 Vecchia, D., Beltramo, R., Vallone, F., Chereau, R., Forli, A., Molano-Mazon, M., Bawa, T., Binini, N.,
661 Moretti, C., Holtmaat, A., Panzeri, S., & Fellin, T. (2020). Temporal Sharpening of Sensory
662 Responses by Layer V in the Mouse Primary Somatosensory Cortex. *Curr Biol*, 30(9), 1589-1599
663 e1510. doi:10.1016/j.cub.2020.02.004
- 664 Wang, Zhang, Z., Chanda, B., & Jackson, M. B. (2010). Improved probes for hybrid voltage sensor
665 imaging. *Biophys J*, 99(7), 2355-2365. doi:10.1016/j.bpj.2010.07.037
- 666 Wang, Y., Gupta, A., Toledo-Rodriguez, M., Wu, C. Z., & Markram, H. (2002). Anatomical,
667 Physiological, Molecular and Circuit Properties of Nest Basket Cells in the Developing
668 Somatosensory Cortex. *Cereb Cortex*, 12(4), 395-410. doi:10.1093/cercor/12.4.395
- 669 Woolsey, T. A., & Van der Loos, H. (1970). The Structural Organization of Layer IV in the
670 Somatosensory Region (S1) of Mouse Cerebral Cortex. *Brain Res*, 17(2), 205-242.
671 doi:10.1016/0006-8993(70)90079-x
- 672 Xu, X., Olivas, N. D., Ikrar, T., Peng, T., Holmes, T. C., Nie, Q., & Shi, Y. (2016). Primary visual cortex
673 shows laminar-specific and balanced circuit organization of excitatory and inhibitory synaptic
674 connectivity. *J Physiol*, 594(7), 1891-1910. doi:10.1113/JP271891

675